

## Hard X-ray Emission Associated with White Dwarfs. IV. Signs of Accretion from Sub-stellar Companions

YOU-HUA CHU,<sup>1</sup> JESÚS A. TOALÁ,<sup>2</sup> MARTÍN A. GUERRERO,<sup>3</sup> FLORIAN F. BAUER,<sup>3</sup> JANA BILIKOVA,<sup>4</sup> AND  
ROBERT A. GRUENDL<sup>4</sup>

<sup>1</sup>*Institute of Astronomy and Astrophysics, Academia Sinica (ASIAA), No.1, Sec. 4, Roosevelt Road, Taipei 10617, Taiwan, ROC*

<sup>2</sup>*Instituto de Radioastronomía y Astrofísica (IRyA), UNAM Campus Morelia, Apartado postal 3-72, 58090 Morelia, Michoacan, Mexico*

<sup>3</sup>*Instituto de Astrofísica de Andalucía, IAA-CSIC, c/Camino Bajo de Huétor 50, E-18008 Granada, Spain*

<sup>4</sup>*Astronomy Department, University of Illinois, Urbana, Illinois 61801, USA*

### ABSTRACT

KPD 0005+5106, with an effective temperature of  $\simeq 200,000$  K, is one of the hottest white dwarfs (WDs). *ROSAT* unexpectedly detected “hard” ( $\sim 1$  keV) X-rays from this apparently single WD. We have obtained *Chandra* observations that confirm the spatial coincidence of this hard X-ray source with KPD 0005+5106. We have also obtained *XMM-Newton* observations of KPD 0005+5106, as well as PG 1159–035 and WD 0121–756, which are also apparently single and whose hard X-rays were detected by *ROSAT* at  $3\sigma$ – $4\sigma$  levels. The *XMM-Newton* spectra of the three WDs show remarkably similar shapes that can be fitted by models including a blackbody component for the stellar photospheric emission, a thermal plasma emission component, and a power-law component. Their X-ray luminosities in the 0.6–3.0 keV band range from  $4 \times 10^{29}$  to  $4 \times 10^{30}$  erg s<sup>-1</sup>. The *XMM-Newton* EPIC-pn soft-band (0.3–0.5 keV) lightcurve of KPD 0005+5106 is essentially constant, but the hard-band (0.6–3.0 keV) lightcurve shows periodic variations. An analysis of the generalized Lomb-Scargle periodograms for the *XMM-Newton* and *Chandra* hard-band lightcurves finds a convincing modulation (false alarm probability of 0.41%) with a period of  $4.7 \pm 0.3$  hr. Assuming that this period corresponds to a binary orbital period, the Roche radii of three viable types of companion have been calculated: M9V star, T brown dwarf, and Jupiter-like planet. Only the planet has a size larger than its Roche radius, although the M9V star and T brown dwarf may be heated by the WD and inflate past the Roche radius. Thus, all three types of companion may be donors to fuel accretion-powered hard X-ray emission.

*Keywords:* (stars:) white dwarfs – X-rays: stars – infrared: stars – stars: individual (KPD 0005+5106, PG 1159–035, and WD 0121–756)

### 1. INTRODUCTION

Three types of X-ray sources are known to be associated with white dwarfs (WDs): (1) photospheric X-ray emission from a WD itself, (2) accretion of material from a close binary companion, as in cataclysmic variables, and (3) coronal X-ray emission from a late-type binary companion, such as dMe stars. The latter two types of sources require the WDs to be in binary systems and their observed X-ray spectra commonly peak near 1 keV or higher, consistent with thermal emission from plasma with temperatures of a few  $\times 10^6$  K. In contrast, the photospheric X-ray emission from a WD is soft and detectable only at photon energies  $< 0.5$  keV. Examples of these different types of sources can be found in *ROSAT* and *XMM-Newton* archival studies of X-ray emission from WDs by O’Dwyer et al. (2003, Paper I),

Chu et al. (2004b, Paper II), and Bilíková et al. (2010, Paper III).

Theoretically, cool WDs with convective envelopes can generate magnetic fields to power coronae and become sources of X-ray emission (Serber 1990; Thomas et al. 1995). Observational searches for coronal emission above a cool WD’s photosphere have thus far failed to provide convincing detections. A stringent upper limit on the X-ray luminosity of a single, cool, magnetic WD has been placed by a 31.8 ks *Chandra* observation of GD 356 to be  $L_X < 6.0 \times 10^{25}$  ergs s<sup>-1</sup> (Weisskopf et al. 2007).

The above conventional wisdom was challenged by the detection of hard (photon energy  $\sim 1$  keV) X-ray emission from apparently single WDs. The most outstanding cases have been WD 2226–216 (the central star of the Helix Nebula; Guerrero et al. 2001) and

KPD 0005+5106 (WD 0005+511), which show a soft photospheric component and a distinct hard component peaking near 1 keV (Paper I). In the case of WD 2226–216, sensitive Hubble Space Telescope observations were used to rule out any companion earlier than M5 (Ciardullo et al. 1999); however, a recent analysis of its TESS lightcurve suggested a  $<0.16 M_{\odot}$  binary companion with an orbital period of 2.77 days (Aller et al. 2020). In the case of KPD 0005+5106, the lack of IR excess and H $\alpha$  emission associated with coronal activity has been used to exclude the existence of a late-type companion with a corona (Chu et al. 2004a).

In Paper I and Paper III, similar hard component peaking near 1 keV has also been detected toward WD 0339–451 at a  $6\sigma$  level, and WD 0121–756 (aka WD 0122–753J, RX J0122–7521), PG 1159–035 (WD 1159–34), and WD 1333+510 at  $3\sigma$ – $4\sigma$  levels; moreover, hard X-ray emission manifested in the soft X-ray emission extending to harder 0.5–1.0 keV photon energy range is observed in WD 1234+481 and WD 1254+223. None of these WDs have known binary companion or show IR excess indicative of a late-type stellar companion. Interestingly, at least four of these WDs have stellar effective temperatures greater than 100,000 K – KPD 0005+5106, WD 0121–756, PG 1159–035, and WD 2226–210.

Spectral and temporal properties of the hard X-ray emission from these intriguing WDs may shed light on the origins of their hard X-rays; however, the existing ROSAT Position Sensitive Proportional Counter (PSPC) observations are of inadequate quality. For example, only  $\sim 10$  photons with energies greater than 0.5 keV were detected in the ROSAT PSPC observations of WD 0121–756 and PG 1159–035 (Paper I, Paper III). Better X-ray observations are needed.

To investigate physical properties of hard X-ray emission from apparently single WDs, we have obtained Chandra X-ray Observatory ACIS-S observation of KPD 0005+5106, but its very luminous soft photospheric emission caused pile-up effects; therefore, we have obtained XMM-Newton observations of KPD 0005+5106 for spectral and temporal analyses. We have also acquired XMM-Newton observations of WD 0121–756 and PG 1159–035 to confirm their hard X-ray emission and to carry out spectral analyses. This paper reports our analyses of these Chandra and XMM-Newton observations: Section 2 describes the X-ray observations as well as complementary IR observations, Sections 3 and 4 report the spectral and temporal analyses of the X-ray data, Section 5 discusses the implications of the X-ray results on the physical origin of the

hard X-ray emission, and finally Section 6 summarizes the conclusion of our study.

## 2. OBSERVATIONS

### 2.1. Chandra X-ray Observation

The Advanced CCD Imaging Spectrometer (ACIS) on board the Chandra X-ray Observatory was used to observe KPD 0005+5106 on 2008 March 19 (Obs. ID 8942; PI: Y.-H. Chu). KPD 0005+5106 was positioned at the aim-point of the ACIS-S array on the back-illuminated CCD S3 and observed in the FAINT mode for a total of 48.0 ks. The data were processed and analyzed using the Chandra Interactive Analysis of Observations (CIAO) software package (version 4.11; Fruscione et al. 2006). The observations were not affected by any period of high background, and no time intervals had to be excised. After dead time correction, the final exposure time was 47.4 ks.

To refine the astrometric accuracy of this Chandra observation, we identified seven X-ray sources with optical counterparts and used their optical positions to calibrate the X-ray astrometry. The final astrometric accuracy of the Chandra observation is better than  $1''$ . A bright X-ray point source is detected at the position of KPD 0005+5106 with a background-subtracted count rate of  $0.157 \pm 0.002$  cts  $s^{-1}$  in the 0.15–4.5 keV energy band.

The background-subtracted ACIS-S spectrum of KPD 0005+5106, shown in Figure 1, exhibits a bright peak near 0.2 keV, a secondary peak near 0.4 keV and a much fainter tertiary peak near 0.6 keV. The bright primary peak corresponds to the soft photospheric emission from KPD 0005+5106. The very high count rate of the primary peak and the locations of the secondary and tertiary peaks suggest that the spectrum is affected by a pileup of photons with energies near the primary peak.

We have thus modeled the pileup effects following guidelines in The Chandra ABC Guide to Pileup<sup>1</sup> provided by the Chandra X-ray Center. This model, plotted over the spectrum in Figure 1, indicates that the pileup contributions are still noticeable up to 0.75 keV.

The pileup-removed, background-subtracted spectrum of KPD 0005+5106, shown in the bottom panel of Figure 1, dips to nearly zero at 0.5 keV, peaks near 1 keV, and diminishes above  $\sim 3$  keV. Its count rate is  $\sim 0.024 \pm 0.001$  cts  $s^{-1}$  in the 0.6–4.5 keV band. Because of the large uncertainties in Chandra ACIS-S calibration below 0.3 keV, the pileup correction is not ideal and the pileup-corrected spectrum of KPD 0005+5106 would not

<sup>1</sup> [http://cxc.harvard.edu/ciao/download/doc/pileup\\_abc.ps](http://cxc.harvard.edu/ciao/download/doc/pileup_abc.ps)

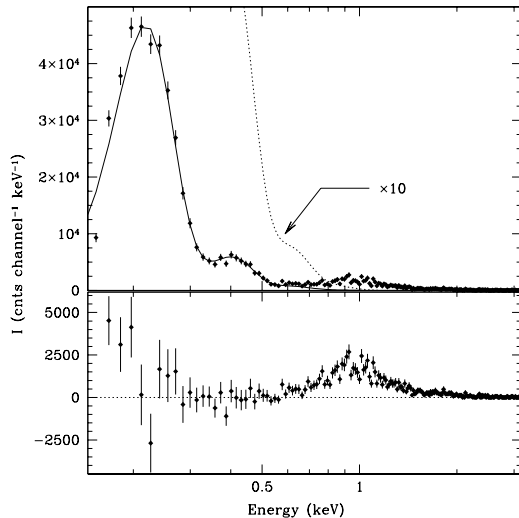


**Figure 1.** Modeling the pileup in the Chandra ACIS-S spectrum of KPD 0005+5106. In the top panel, the data points with error bars show the background-subtracted raw spectrum, the solid curve shows a pileup model for the spectrum, and the pileup model multiplied by a factor of 10 is plotted in a dotted curve to show the low-level effect near 0.6 keV. The bottom panel shows the pileup-removed background-subtracted ACIS-S spectrum.

be suitable for spectral analysis. We will nevertheless use the Chandra ACIS-S data to extract lightcurves in the hard X-ray band ( $\geq 0.75$  keV, free of pileup effects) for comparisons with those extracted from the XMM-Newton observations.

## 2.2. XMM-Newton X-ray Observations

We obtained pointed XMM-Newton observations for KPD 0005+5106, WD 0121–756, and PG 1159–035 with the European Photon Imaging Cameras (EPIC) in 2012 November and December (PI: Y.-H. Chu). The Obs. IDs are 0693050401, 0693050501, and 0693050601, and the exposure times are 35.7 ks, 15.4 ks, and 10.4 ks, respectively. To avoid pileup, the Small Window mode and the Medium filter were used in the observations. The Small Window mode reads out every 5.7 ms, and only count rates higher than  $25 \text{ counts s}^{-1}$  cause pileup. In addition, we find in the XMM-Newton archive two observations that include PG 1159–035 in the EPIC’s field of view. These two observations’ target was the Seyfert-type galaxy Mrk 1310, but PG 1159–035 is located  $\sim 8$ – $9$  arcmin from the aim point (depending on the EPIC camera). Thus, these two observations, Obs. ID 0723100301 (PI: N. Shartel) and 0831790501 (PI: B. Kelly), have been used to complement our observations of PG 1159–035. Details of all the EPIC observations used in this paper are listed in Table 1, where the EPIC-

pn, MOS1, and MOS2 cameras are denoted as pn, M1, and M2, respectively.

The EPIC observations were processed with the XMM-Newton Science Analysis Software (SAS version 17.0) with the calibration files from 2019 June 13. To avoid periods of high background, we extracted lightcurves of the whole field in the 10–12 keV energy range using 100 s time bins, and excised time intervals with high count rates in this high energy band. The resultant useful times for each observation and camera are listed in Table 1 as net exposure times.

Individual spectra were extracted from each of the pn and MOS observations using the SAS task *evselect*. To extract the spectra of a WD, a circular source aperture of  $20''$  and a surrounding or nearby background region devoid of sources were used. Their corresponding calibration matrices, redistribution matrix file (rmf) and auxiliary response file (arf), were produced with the SAS tasks *rmfgen* and *arfgen*. Background-subtracted source count rates of each camera obtained from different observations are listed in the last three columns of Table 1.

EPIC spectra extracted from different cameras were combined to produce a single EPIC spectrum for each WD. This has been done by making use of the SAS task *epicspeccombine*. This task creates a single background-subtracted spectrum for each source plus corresponding calibration matrices<sup>2</sup>. The resultant combined EPIC spectra of KPD 0005+5106, PG 1159–035, and WD 0121–756, are presented in Figure 2.

## 2.3. Infrared Observations

The Multiband Imaging Photometer for Spitzer (MIPS; Rieke et al. 2004) on board the Spitzer Space Telescope was used to image KPD 0005+5106 in the 24 and  $70 \mu\text{m}$  bands (Program ID 40953; PI: Y.-H. Chu). Images were obtained in photometry mode with the small offset scale and 10 s exposure time for three cycles at both 24 and  $70 \mu\text{m}$ . The Basic Calibrated Data processed by the Spitzer Science Center’s pipeline software were used to construct mosaics in each band using utilities in the MOPEX software package. Prior to building each mosaic, bad pixels and latent images of bright point sources were flagged and removed, and the background brightness offsets between the individual frames were adjusted and removed.

KPD 0005+5106 was not detected at either  $24 \mu\text{m}$  or  $70 \mu\text{m}$ . We used the PHOT package in IRAF to obtain estimates for the  $3\sigma$  detection limit in these two MIPS

<sup>2</sup> See the *epicspeccombine* thread in <https://www.cosmos.esa.int/web/xmm-newton/sas-thread-epic-merging>

**Table 1.** XMM-Newton Observations of Three Apparently Single WDs with Hard X-ray Emission

Object	Obs. ID.	Date (yyyy-mm-dd)	Total Exposure Time			Net Exposure Time			Source Count Rate		
			pn (ks)	M1 (ks)	M2 (ks)	pn (ks)	M1 (ks)	M2 (ks)	pn (counts ks <sup>-1</sup> )	M1	M2
KPD 0005+5106	0693050401	2012-12-31	35.3	34.3	34.3	35.2	34.3	34.3	60.2	17.4	18.6
WD 0121-756	0693050501	2012-11-26	15.0	15.1	15.1	6.0	12.0	12.5	14.0	4.1	3.5
PG 1159-035	0693050601	2012-12-12	10.0	10.1	10.1	5.0	9.5	9.8	7.5	2.3	1.2
PG 1159-035	0723100301	2013-12-09	...	51.2	51.2	...	33.7	31.0	...	0.8	1.3
PG 1159-035	0693050601	2019-01-04	24.2	26.0	26.0	18.3	25.2	24.2	5.8	1.7	1.2

Note: The three EPIC cameras are denoted as pn, M1, and M2. The EPIC-pn observation 0723100301 was performed in the small window mode and did not encompass PG 1159-035.

bands and find flux density limits of  $<0.11$  and  $<14.2$  mJy at 24 and 70  $\mu\text{m}$ , respectively. These limits are too shallow to provide useful constraints on faint binary companions.

Spitzer InfraRed Array Camera (IRAC; Fazio et al. 2004) observations of KPD 0005+5106 were made in the 4.5 and 8.0  $\mu\text{m}$  bands, and the flux densities were reported to be  $297.5 \pm 9.9$  and  $96 \pm 14$   $\mu\text{Jy}$ , respectively (Mullally et al. 2007). These values will be used in our analysis in Section 5.3.3.

Near-IR  $JHK_s$  observations of KPD 0005+5106 were also obtained with the Near Infrared Camera Spectrometer (NICS) on the 3.58 m Telescopio Nazionale Galileo (TNG) on 2008 October 12-13. The detector was a HgCdTe Hawaii 1024 $\times$ 1024 array with a 4'2 $\times$ 4'3 field of view. The night was clear and photometric. KPD 0005+5106 was observed at three epochs: October 12 at UT = 19.4 h and October 13 at UT = 0.3 and 1.7 h. At each epoch seven 50 s frames were obtained in each of the  $J$ ,  $H$ , and  $K_s$  bands. No systematic variations are seen among the 21 measurements in each band, and their averages are  $J = 14.07 \pm 0.04$ ,  $H = 14.15 \pm 0.03$ , and  $K_s = 14.26 \pm 0.07$ . These values can be compared with the 2MASS measurements (2MASS J00081816+5123165) of  $J = 13.95 \pm 0.03$ ,  $H = 14.14 \pm 0.04$ , and  $K_s = 14.19 \pm 0.06$ . The  $J$  magnitude shows a  $\sim 2\sigma$  difference, but the  $H$  and  $K_s$  magnitudes are constant. No large long-term variations are present.

### 3. X-RAY SPECTRAL ANALYSES

The XMM-Newton EPIC spectra, shown in Figure 2, clearly detect the hard X-ray emission peak near 1 keV in all three WDs, confirming the previous ROSAT PSPC's  $3\sigma$  detection at 10 counts for PG 1159-034, and WD 0121-756. The spectra of the three WDs are amazingly similar, showing a soft component below 0.4 keV rising toward lower energies and a hard component peaking near  $\sim 1$  keV and extending to higher energies. In the high-quality spectrum of KPD 0005+5106, even

some line features are discernible in the 0.5 to 0.9 keV range.

To gain insight into physical properties and origin of the X-ray emission from these apparently single WDs, we analyze their EPIC spectra with XSPEC (version 12.10.1; Arnaud 1996). We consider three types of emission – blackbody model for stellar photospheric emission, thermal plasma emission model, and power-law model for nonthermal emission. All these emission models are absorbed using a *tbabs* model as described in Wilms et al. (2000) and included in XSPEC. Initially, we model the spectra with two emission components, a blackbody component for the WD's photospheric emission and an optically thin plasma emission component or a nonthermal power-law component. None of the two-component models can successfully fit the EPIC spectra; they all result in reduced  $\chi^2$  greater than 2. Thus, more complex models need to be considered.

As the EPIC spectrum of KPD 0005+5106 has the highest quality and shows line features in hard X-rays (see Fig. 2 - left panel), we start detailed spectral modeling of this spectrum by including (1) a blackbody component for the WD's photospheric emission with temperature fixed at the effective temperature of KPD 0005+5106,  $T_{\text{eff}} = 2 \times 10^5$  K (Werner et al. 2008; Wassermann et al. 2010); (2) a thermal plasma emission component for the line features; and (3) a thermal plasma or power-law component to improve the spectral fits.

For the three-component fits to KPD 0005+5106's spectrum, we first consider another plasma emission model for the third component, i.e., using the above fixed-temperature blackbody emission model plus two optically thin *apec* plasma emission models. The absorption column density as well as the plasma temperatures of the two *apec* models are left as free parameters. The best-fit model to the spectrum, with plasma temperatures of  $kT_1=0.20$  keV and  $kT_2=0.62$  keV and an unre-

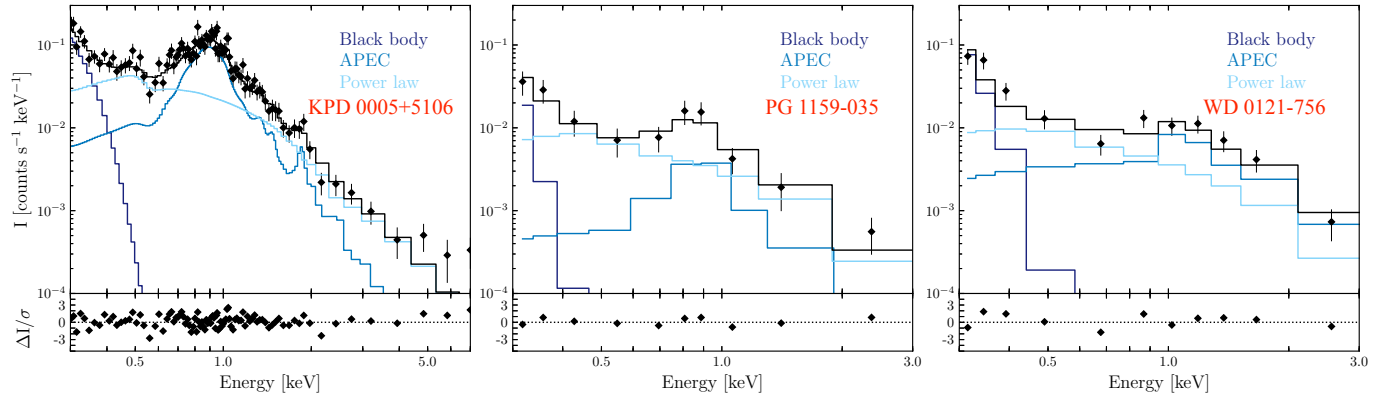


**Figure 2.** XMM-Newton EPIC spectra of KPD 0005+5106, PG 1159–035, and WD 0121–756. The best-fit model to the data is plotted in solid black line. The contributions from the black body, *apec*, and power-law components are plotted in different shades of blue lines.

**Table 2.** Best-fit parameters to the EPIC spectra

Object	$N_{\text{H}}$ ( $\times 10^{20}$ cm $^{-2}$ )	$T_{\text{eff}}$ ( $\times 10^5$ K)	$kT$ (keV)	$\Gamma$	$F_{\text{X,TOT}}$ (erg s $^{-1}$ cm $^{-2}$ )	$L_{\text{X,TOT}}$ (erg s $^{-1}$ )	$L_{\text{apec}}/L_{\text{X,TOT}}$	$L_{\text{pow}}/L_{\text{X,TOT}}$
KPD 0005+5106	$9_{-7}^{+5}$	<b>2.0</b>	$0.84_{-0.03}^{+0.07}$	$2.9_{-0.4}^{+0.4}$	$4.8 \times 10^{-13}$	$8.7 \times 10^{30}$	0.18	0.27
PG 1159–035	<b>2.0</b>	<b>1.4</b>	$0.86_{-0.30}^{+0.45}$	<b>3.0</b>	$1.3 \times 10^{-14}$	$4.7 \times 10^{29}$	0.16	0.66
WD 0121–756	<b>4.0</b>	<b>1.8</b>	$2.00_{-0.65}^{+2.00}$	<b>3.0</b>	$9.2 \times 10^{-14}$	$8.7 \times 10^{30}$	0.17	0.20

Note: Boldface text correspond to fixed values during the spectral fit. Fluxes and luminosities have been computed in the 0.3–3.0 keV energy range for PG 1159–035 and WD 0121–756, but in the 0.3–7.0 keV for KPD 0005+5106.

alistically low absorption column density, has a reduced  $\chi^2$  of 2.5 and hence is still not formally acceptable.

We then consider a power-law model for the third component, i.e., using a fixed-temperature blackbody component, an *apec* plasma emission component, and a power-law component. The best-fit model to KPD 0005+5106’s spectrum has a plasma temperature of  $kT=0.84_{-0.03}^{+0.07}$  keV, a power-law index of  $\Gamma = 2.9_{-0.4}^{+0.4}$ , and an absorption column density of  $N_{\text{H}} = (9_{-7}^{+5}) \times 10^{20}$  cm $^2$ , consistent with estimates from the Ly $\alpha$  absorption profile (Werner et al. 1994); furthermore, the reduced  $\chi^2$  is improved to 1.16. We consider this best-fit model acceptable. The best-fit model’s three individual emission components and their sum are plotted over the background-subtracted EPIC spectrum of KPD 0005+5106 in the leftmost panel of Figure 2. It can be seen that the blackbody component of the photospheric emission dominates the spectrum at energies below 0.4 keV. The *apec* plasma emission component contributes to the broad peak around 1 keV and the emission line feature at  $\sim 1.8$  keV, which is likely a Si VIII line. The power-law component dominates at high energies from 2 keV up to 5–6 keV, as well as

the intermediate energies at 0.4–0.6 keV. The intrinsic (unabsorbed) flux in the 0.3–7.0 keV energy range is  $F_{\text{X}} = 4.8 \times 10^{-13}$  erg s $^{-1}$  cm $^{-2}$ , corresponding to an X-ray luminosity of  $L_{\text{X}} = 8.7 \times 10^{30}$  erg s $^{-1}$  at the distance of  $387 \pm 8$  pc adopted from the Gaia data release 2 (Gaia Collaboration et al. 2018). Detailed parameters of the best-fit model are given in Table 2.

We note that multi-temperature plasma emission models also produce acceptable fits to the EPIC spectrum of KPD 0005+5106. For example, we have fitted the EPIC spectrum with a blackbody component plus three *apec* components. This results in a reasonably good fit ( $\chi^2=1.5$ ) with plasma temperatures of  $kT_1 = 0.05_{-0.007}^{+0.02}$  keV,  $kT_2 = 0.82_{-0.05}^{+0.01}$  keV, and  $kT_3 = 2.6_{-0.5}^{+1.0}$  keV. The highest temperature component is needed for the X-ray emission above  $\sim 1.5$  keV and the lowest temperature component is needed for the X-ray emission around 0.4–0.6 keV. The spectral fits can be further improved ( $\chi^2=1.1$ –1.3) if more plasma components are added. Based on Occam’s Razor, we do not pursue multi-temperature plasma model fits further; however, as we show in Section 4, multiple temperatures

may be needed to explain the temporal variations of the spectral properties.

Following our spectral analysis of KPD 0005+5106, we find that the spectra of PG 1159–035 and WD 0121–756 similarly need to be modeled by a blackbody component, an *apec* thermal plasma component, and a power-law component. These two WDs are fainter and have shorter exposure times; thus their observations detected much fewer counts than KPD 0005+5106 and their spectra do not allow fitting many free parameters simultaneously. We have converted these two WDs’ extinction measurements into H column densities and adopt them as fixed absorption column densities  $N_{\text{H}}$ , which are  $2 \times 10^{20} \text{ cm}^{-2}$  and  $4 \times 10^{20} \text{ cm}^{-2}$  for PG 1159–035 (Dreizler, & Heber 1998) and WD 0121–756 (van Teeseling et al. 1996), respectively. The blackbody components’ temperatures are fixed at the effective temperatures of the WDs,  $1.4 \times 10^5 \text{ K}$  for PG 1159–035 (Dreizler, & Heber 1998) and  $1.8 \times 10^5 \text{ K}$  for WD 0121–756 (Werner et al. 1996). We also adopt the best-fit  $\Gamma$  of KPD 0005+5106 and fix the  $\Gamma$  of PG 1159–035 and WD 0121–756 at 3.

The resultant best-fit models for PG 1159–035 ( $\chi^2 = 1.20$ ) and WD 0121–756 ( $\chi^2 = 1.9$ ) are listed in Table 2 and plotted over their background-subtracted EPIC spectra in Figure 2. It can be seen that the three components’ contributions to PG 1159–035 in different energy ranges are very similar to those to KPD 0005+5106. WD 0121–756, on the other hand, appears to have the power-law component dominating in the 0.4–0.7 keV energy range, while the plasma emission component dominates in the 1–3 keV energy range. Note that this dominance of plasma emission in hard X-rays may be caused by a higher plasma temperature in the best-fit model of WD 0121–756,  $kT = 2 \text{ keV}$ , instead of the  $kT \sim 0.85 \text{ keV}$  for KPD 0005+5106 and PG 1159–035. Better spectral qualities are needed to confirm this result. It is nevertheless interesting to note that the power-law component makes the most significant contribution to the spectrum in the 0.4–0.6 keV energy range.

#### 4. TEMPORAL VARIATIONS OF HARD X-RAYS

Among the three WDs observed with XMM-Newton, only KPD 0005+5106 had high enough a count rate and long enough an exposure time (see Table 1) to warrant temporal variation analyses. We first extracted background-subtracted lightcurves from the EPIC pn observation in three different energy ranges: the entire 0.2–3.0 keV energy band that covers the bulk of X-ray emission, the soft X-ray band of 0.2–0.5 keV, and a hard band covering the 0.6–3.0 keV energy range. We have also extracted a lightcurve from the Chandra ACIS-S observation. As stated in Section 2.1, the pileup effect

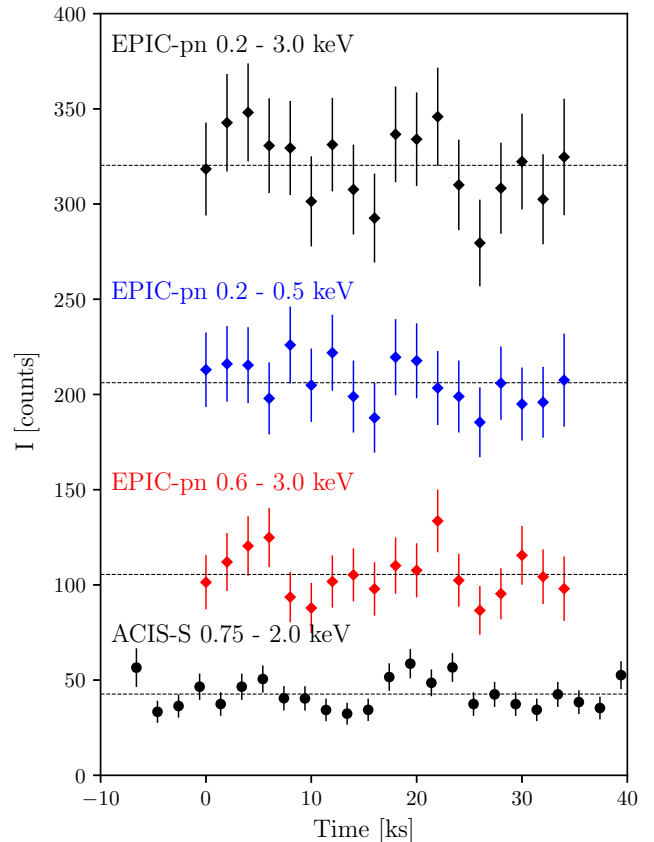


**Figure 3.** Background-subtracted EPIC and ACIS-S lightcurves of KPD 0005+5106. Each bin corresponds to 2 ks. The dashed thin lines represent the average values.

is negligible compared with the WD’s hard X-ray emission at photon energies greater than  $\sim 0.7 \text{ keV}$ . Thus, we extracted a lightcurve in the 0.75–2.0 keV energy range from the Chandra ACIS-S observations. All four lightcurves are presented in Figure 3.

The EPIC-pn lightcurves show a weak hint of variations in the broad band (0.2–3.0 keV) and essentially no variations in the soft band (0.2–0.5 keV); however, variations are visible in the hard band (0.6–3.0 keV) and the two peaks are separated by  $\sim 18 \text{ ks}$  ( $= 5 \text{ hr}$ ). The ACIS-S lightcurve in the hard band (0.75–2.0 keV) shows similar variations. If the ACIS-S lightcurve is shifted to align its clearest peak with the EPIC-pn hard-band lightcurve peak at 20 ks, it can be seen that ACIS-S lightcurve also shows a lower peak at  $\sim 4 \text{ ks}$  mark where the EPIC-pn hard-band lightcurve peaks. The similarity between these two hard-band lightcurves lends support to the apparent 18 ks period in the lightcurve. To assess the significance of this periodic variation, we performed

Kolmogorov-Smirnov tests to the data and found the variation more likely to be real than statistical fluctuations. Thus, we performed more rigorous analysis using both ACIS-S and EPIC-pn data as described below.

We first normalized the Chandra ACIS-S and XMM-Newton EPIC-pn hard-band lightcurves by their respective median flux values, then computed the generalized Lomb-Scargle periodograms (Zechmeister & Kürster 2009) to find periodicities in these unequally spaced data and the false alarm probabilities (FAPs). We carried out computations for these two data sets both individually and combined. The results are shown in the left panel of Figure 4, with the generalized Lomb-Scargle periodograms of the Chandra data in blue, XMM-Newton data in orange, and the combined data in black. Both Chandra and XMM-Newton data independently show periodic variations close to 5 hr (frequency  $\sim 5 \text{ day}^{-1}$ ), although each data set covers only 2-3 cycles of this modulation. The combined data set covers 4.6 cycles, and its X-ray intensity modulation for a period of  $4.7 \pm 0.3$  hr should be more robust. The error bar is estimated at 1% FAP. Indeed, the FAP decreases from 10% for the Chandra data and 2% for the XMM-Newton data, to 0.41% for the combined data set. The Chandra and XMM-Newton lightcurves folded to 4.7 hr, displayed in the right panel of Figure 4, show similar shapes within the error limits.

To investigate whether the X-ray spectral properties vary between the high state and low state of KPD 0005+5106, we have extracted an EPIC-pn spectrum from time intervals near the peaks in the hard-band lightcurve, and another EPIC-pn spectrum from time intervals near the valleys of the hard-band lightcurve. The two spectra, shown in Figure 5, are statistically similar at energies below 0.5 keV, but the high-state spectrum is brighter than the low-state spectrum, which is not surprising as the high-state and low-state spectra correspond to peaks and valleys of the lightcurve, respectively.

To quantify the differences between the high- and low-state EPIC-pn spectra, we have modeled them with three components (blackbody + thermal plasma + power law) as discussed in length in Section 3. Although the resultant best-fit models for the high- and low-state spectra are suggestive of small variations in the plasma temperature and the power-law photon index  $\Gamma$ , they are also consistent within their error bars. It is nevertheless clear that the best-fit models indicate the high-state is 1.5 times as bright as the low-state regime.

We note that in addition to the obvious luminosity differences, there are subtle differences in the line features. For example, compared with the low-state spectrum, the

high-state spectrum shows a stronger contribution from Ne lines at  $\sim 1.0$  keV and an excess at  $\lesssim 1.4$  keV probably due to the Mg XI line emission at a  $2-3\sigma$  confidence level. Moreover, the low-state spectrum exhibits an emission peak near 0.5 keV that is also present in the EPIC spectrum in Figure 2 but not seen in the high-state spectrum. It would be very interesting to analyze detailed differences between the high- and low-state spectra, for example, plasma temperatures and abundances, the number of thermal plasma components needed in spectral fits, and their relative contributions (see Section 3); however, the current data do not have adequate counts and resolution for such analyses. Future deeper observations would be desirable.

## 5. DISCUSSION

We first use the positional coincidence to affirm the physical association between the hard and soft X-ray emission components in the WDS, then compare the spectral properties among the three WDS, and discuss the possible origins of the hard X-ray emission.

### 5.1. *Spatial Coincidence between the Hard and Soft X-ray Emission*

The superb angular resolution of Chandra enables us to determine accurately whether a position offset exists between the hard and soft X-ray emission from KPD 0005+5106. We have extracted images of KPD 0005+5106 in a soft band (0.2–0.5 keV) and a hard band (0.8–3.5 keV), and find that the soft and hard X-ray point sources are coincident with each other (in the same  $0''.5$  pixel) and with the optical position of the WD (within  $1''$ ). These coincidences support that both the soft and hard X-ray components are attributed to KPD 0005+5106.

The angular resolution of XMM-Newton is not as good as Chandra, yet it can still be shown from the pointed observations of PG 1159–035 and WD 0121–756 that both their hard and soft X-ray components and the optical position of the WD are coincident with one another within  $\sim 1''$ . We therefore consider that the spatial coincidences affirm the physical association between the hard and soft X-ray components and between the X-ray emission and the WD.

### 5.2. *Similarities among the Three WDS*

KPD 0005+5106 is a DO WD, while PG 1159–035 and WD 0121–756 are PG 1159 type WDS. Both DO and PG 1159 spectral types imply a H-deficient, He-rich atmosphere. Besides the similarity in composition, all three have stellar effective temperatures greater than 100,000 K: 200,000 K, 140,000 K, and 180,000 K for

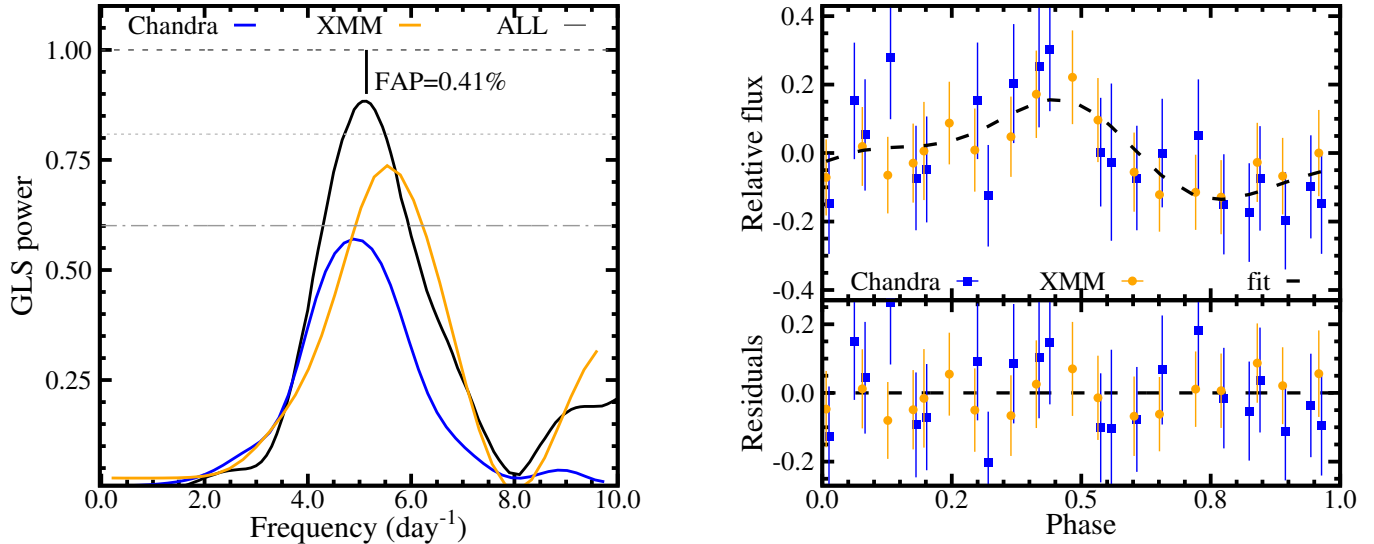


**Figure 4.** Left panel: Generalized Lomb-Scargle (GLS) periodograms of Chandra ACIS-S data (blue), XMM-Newton EPIC-pn data (orange), and the combined data set (black). False alarm probabilities (FAP) of 10%, 1%, and 0.1% are indicated by dash-dotted, dotted, and dashed grey lines, respectively. Right panel: Phase-folded X-ray lightcurves of Chandra ACIS-S data (blue squares), XMM-Newton EPIC-pn data (orange dots) and a spline model fit (black dashed line).

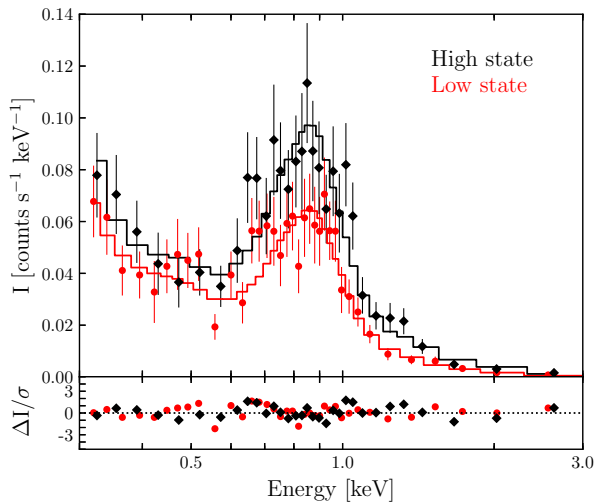


**Figure 5.** Background-subtracted EPIC pn spectra extracted from time intervals in the high and low states, plotted in black and red, respectively.

KPD 0005+5106, PG 1159–035, and WD 0121–756, respectively.

The X-ray spectral properties of the three WDs are also similar. As analyzed in Section 3, all three WDs have similar X-ray spectral shapes. They all possess a soft X-ray component corresponding to the stellar photospheric emission and hard X-rays peaking near 1 keV. Furthermore, the hard X-ray emission cannot be fitted well by two thermal plasma emission components; in-

stead, it requires models consisting of a thermal plasma emission component and a power-law component (or multi-temperature plasma components).

These similarities in physical properties of the WDs and in X-ray spectral properties suggest that all three WDs may share a common origin for their hard X-ray emission.

### 5.3. Origin of the Hard X-ray Emission

We will consider three possible origins of the observed hard X-rays from these apparently single WDs: (1) photospheric emission, (2) hidden coronal companion, and (3) accretion from a hidden companion.

#### 5.3.1. Photospheric Emission

KPD 0005+5106 is the most well-studied and its X-ray spectrum has the highest quality among the three WDs reported in this paper. We will thus first examine previous studies of KPD 0005+5106 in detail.

KPD 0005+5106 is such a bright soft X-ray source that it was detected in the ROSAT All Sky Survey. Fleming et al. (1993) showed that the spectrum of KPD 0005+5106 in the 0.1–0.4 keV range could be fitted by a model of thermal plasma at a temperature of  $2.6 \times 10^5$  K, and suggested that its X-ray emission originated from a corona cooler than those of typical main-sequence stars. A corona for KPD 0005+5106 would be surprising because the star is fully ionized and should not have a convective envelope to power a corona. Indeed, based on a Chandra Low Energy



Transmission Grating Spectrograph (LETGS) observation, Drake & Werner (2005) found that the X-ray spectrum of KPD 0005+5106 at 20–100 Å (0.12 – 0.62 keV) could be better modeled as photospheric emission with effective temperature of 120,000 K and  $\log g = 7$ . They ruled out coronal emission as the X-ray source because the extrapolated optical continuum intensity would exceed the observed photospheric continuum, and because of a lack of H-like and He-like C lines that should otherwise have been observed in X-rays. Their 120,000 K photosphere model can explain the soft X-ray spectrum, but cannot reproduce the hard X-ray emission from KPD 0005+5106.

The discovery of photospheric Ca X emission lines in the Far Ultraviolet Spectroscopic Explorer (FUSE) spectrum, in conjunction with the Ne VIII lines in UV and optical spectra, provided evidence that KPD 0005+5106 has an effective temperature of  $\sim 200,000$  K, much hotter than previous estimates (Werner et al. 2007, 2008). In light of this higher temperature, the stellar spectrum of KPD 0005+5106 has been re-modeled by Wassermann et al. (2010). The new model not only has a higher temperature but also higher metallicities than those in the model of Drake & Werner (2005). Despite its higher temperature, this new model cannot reproduce the observed hard X-ray emission from KPD 0005+5106.

We conclude that the hard X-ray emission from KPD 0005+5106 does not have a photospheric origin. This conclusion may apply to PG 1159–035 and WD 0121–756 as well.

### 5.3.2. Hidden Companions with Active Coronae

Previously, Chu et al. (2004a) assumed the hard X-ray emission of KPD 0005+5106 originated completely from a coronal companion, and showed that such companion would outshine the WD itself in near-IR passbands. Here we use a similar but more systematic approach to examine the possible presence of hidden companions.

To assess the possibility that the hard X-ray emission from KPD 0005+5106, PG 1159–035, and WD 0121–756 originates from the coronal activity of late-type dwarf companions, we first compare the brightness of the WD with a potential companion in the  $K$  band to see whether a companion can hide underneath the bright WD emission. We have computed the expected  $m_K$  magnitudes of K0, K5, M0, M5, and M8 dwarf stars at the distances of KPD 0005+5106 (390 pc), PG 1159–035 (550 pc), and WD 0121–756 (890 pc), using the standard star magnitudes from Schmidt-Kaler (1982) and distances from Gaia data release 2 (Gaia Collaboration et al. 2018). The expected

$m_K$  magnitudes of these stars, as well as the observed  $K$  magnitudes the WDs, are listed in Table 3. Obviously, a bright companion cannot hide behind a fainter WD; thus only the latest type of M dwarfs are candidates of hidden companions.

We next consider whether coronae of late-type companions are able to provide the hard X-ray luminosities of these three WDs:  $3.9 \times 10^{30}$ ,  $3.9 \times 10^{29}$ , and  $3.2 \times 10^{30}$  erg s $^{-1}$  for KPD 0005+5106, PG 1159–035, and WD 0121–756, respectively. We computed  $\log(L_X/L_{\text{bol}})$  for the putative late-type dwarf companions, and listed them in Table 3, too. The highest  $\log(L_X/L_{\text{bol}})$  observed in K–M dwarf stars with saturated coronal activity is about  $-3.5$ , and some flare stars can reach  $-2.8$  (Fleming et al. 1995; Güdel 2004). The values of  $\log(L_X/L_{\text{bol}})$  listed in Table 3 indicate that these late type dwarf stars would have  $\log(L_X/L_{\text{bol}})$  exceeding the range, up to about  $-3$ , that can possibly be provided by stellar coronae.

Figure 6 is another presentation comparing the brightness and  $\log(L_X/L_{\text{bol}})$  of putative late-type dwarf companions with those of the WD. All K0–M8 dwarf stars are either too bright in the  $K$  band and/or cannot provide the observed hard X-ray luminosities. Therefore, we can rule out coronal activities of a late-type companion for the origin of the hard X-ray emission detected in KPD 0005+5106, PG 1159–035, and WD 0121–756.

### 5.3.3. Accretion from a Hidden Companion

Finally we consider accretion-powered hard X-ray emission from the WDs. We will use KPD 0005+5106 as an example for our analysis, as it has the most well determined physical parameters among the apparently single WDs with hard X-ray emission. We adopt a mass of  $0.64 M_{\odot}$  and a radius of  $0.059 R_{\odot}$  (or  $6.5 R_{\oplus}$ ) for KPD 0005+5106 (Wassermann et al. 2010).

We use the Spitzer IRAC observations and the 2MASS, or TNG NICS,  $JHK_s$  observations of KPD 0005+5106 to place constraints on possible companions. The  $B$  and  $V$  magnitudes of KPD 0005+5106 have been measured by Downes et al. (1985):  $B = 13.02$  and  $V = 13.32$ . These optical and IR photometric measurements are used to produce the spectral energy distribution (SED) of KPD 0005+5106 shown in Figure 7, where the model spectrum from Wassermann et al. (2010) is also plotted. The extinction correction has been made by using the hydrogen column density of  $N_{\text{H}} = 5 \times 10^{20}$  H-atoms cm $^{-2}$  toward KPD 0005+5106 (Werner et al. 1994) and the gas-to-dust ratio of  $N_{\text{H}}/E(B - V) = 5.8 \times 10^{21}$  H-atoms cm $^{-2}$  mag $^{-1}$  (Bohlin et al. 1978).

**Table 3.** Infrared and X-ray Properties of Putative Late-type Dwarf Companions

Spectral Type	KPD 0005+5106		PG 1159-035		WD 0121-756	
	$m_k$	$\log(L_X/L_{\text{bol}})$	$m_k$	$\log(L_X/L_{\text{bol}})$	$m_k$	$\log(L_X/L_{\text{bol}})$
K0	11.90	-2.62	12.64	-3.62	13.69	-2.70
K5	12.46	-2.17	13.20	-3.17	14.25	-2.26
M0	13.11	-1.88	13.85	-2.88	14.90	-1.97
M5	14.09	-1.03	14.83	-2.03	15.88	-1.12
M8	15.26	-0.07	16.00	-1.07	17.05	-0.16
WD	14.19±0.06		15.73±0.23		16.21±...	

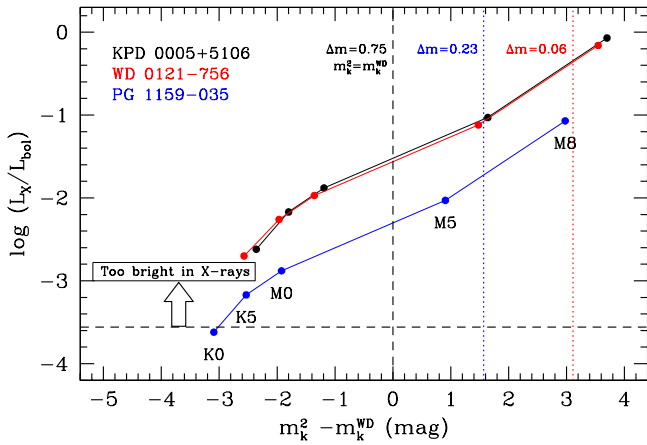


**Figure 6.** X-ray to bolometric luminosity ratio and infrared excess in the  $K$  band of putative late-type dwarf companions of KPD 0005+5106 (black), PG 1159-035 (blue), and WD 0121-756 (red). The different spectral types have been connected by dotted lines for each WD and are labeled in the track of PG 1159-035. Dots to the left of the vertical dashed line imply that putative late-type dwarf companions would be actually brighter than the observed  $m_K$  magnitudes of KPD 0005+5106 (14.26), PG 1159-035 (15.733), and WD 0121-756 (16.213). Dots above the horizontal dashed line imply that putative late-type dwarf companions would have actually X-ray to bolometric luminosity ratios in excess of the canonical value for saturated activity in these stars.

Comparing the observed SED with these model SEDs (Fig. 7, see figure caption for origin of data and references), we can easily rule out the existence of a companion of spectral type M5 or earlier. The observed 4.5 and 8.0  $\mu\text{m}$  fluxes are  $\sim 20\%$  lower than those expected

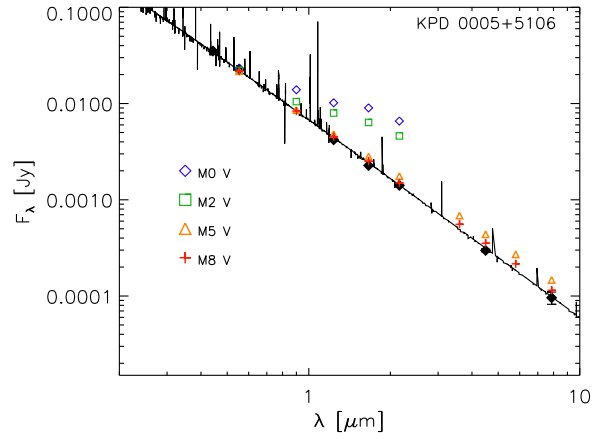


**Figure 7.** Spectral energy distribution (SED) of KPD 0005+5106. The solid symbols are data:  $B$  and  $V$  (Downes et al. 1985; McCook & Sion 1999), 2MASS  $J$ ,  $H$ , and  $K_s$ , Spitzer IRAC 4.5 and 8  $\mu\text{m}$  (Mullally et al. 2007). The error bars are all smaller than the symbols, except the 8  $\mu\text{m}$  measurement. The open symbols are models assuming M-type companions. The photometry of standard M stars are from Kirkpatrick & McCarthy (1994) and Patten et al. (2006). The solid curve is a model SED of KPD 0005+5106 from Wassermann et al. (2010) normalized to the  $K_s$  band.

with an M8 V companion. Suffice it to say, any hidden companion of KPD 0005+5106 has to be fainter and less massive than an M8 V star.

We will consider three types of hidden companions, an M9 V star with a mass of  $0.075 M_\odot$  and a radius of  $0.08 R_\odot$  (Kaltenegger & Traub 2009), a T type brown dwarf with a mass of  $0.035 M_\odot$  and a radius of  $\sim 0.1 R_\odot$ , and a Jupiter-like planet with a mass of  $0.001 M_\odot$  and a radius of  $\sim 0.1 R_\odot$ . We assume that the period of 4.7 hr in the lightcurve of KPD 0005+5106's hard X-ray emission is the orbital period of this binary system. Using the Kepler's third law, we can determine the separation between the WD and the companion,  $1.27 R_\odot$  for a M9 V star,  $1.24 R_\odot$  for a T brown dwarf, and  $1.22 R_\odot$  for a

Jupiter-like planet. The effective Roche radius  $r_L$  of the companion can be approximated by:

$$r_L/a = \frac{0.49 q^{2/3}}{0.6 q^{2/3} + \ln(1 + q^{1/3})}, \quad (1)$$

where  $a$  is the separation between the WD and the companion and  $q$  is the companion to WD mass ratio (Eggleton 1983). We find Roche radii of  $0.28 R_\odot$ ,  $0.21 R_\odot$ , and  $0.067 R_\odot$  for a M9 V star, a T brown dwarf, and a Jupiter-like planet, respectively. Comparing these Roche radii with their respective radii, it is clear that a Jupiter-like planet is larger than the Roche radius and can channel mass to the WD easily. The atmospheres of M9 V star and T brown dwarf, being ionized and heated by the 200,000 K KPD 0005+5106 at a distance of  $\sim 1.3 R_\odot$ , may be inflated and the outer edge of their atmospheres may exceed the Roche radius and be accreted by the the WD. We conclude that all three types of hidden companions may be the donor providing material for accretion-powered hard X-ray emission, although a Jupiter-like planet can do it most easily.

Previously,  $\sim 10$  WDs accreting from brown dwarfs have been reported (Longstaff et al. 2019). Only two of them show X-ray emission, EF Eridani (Schwope et al. 2007) and SDSSJ121209.31+013627.7 (Stelzer et al. 2017); however, both are cool WDs with effective temperatures lower than 10,000 K, and both are polars whose strong magnetic fields channel material from the companion to the WDs' magnetic poles to be accreted. The three WDs with hard X-ray emission reported in this paper have much higher effective temperatures than these polars. As noted above, these hot WDs can accrete material from either a Jupiter-like planet or an irradiated brown dwarf, and hence are very different from the polars.

If we assume that the hard X-ray emission is powered by accretion from a companion, then the accretion rate would be  $L_X R_{WD} / (GM_{WD})$ , where  $L_X$  is the hard X-ray luminosity,  $R_{WD}$  and  $M_{WD}$  are the radius and mass of the WD, and  $G$  is the gravitational constant. For KPD 0005+5106's hard X-ray luminosity ( $3 \times 10^{30}$  ergs  $s^{-1}$ ), mass, and radius, the mass accretion rate would need to be  $2.3 \times 10^{-12} M_\odot \text{ yr}^{-1}$ , or  $1.45 \times 10^{14} \text{ g s}^{-1}$ . This mass accretion rate is very small that a Jupiter-like planet donor may survive for a few times  $10^8$  yr.

It ought to be noted that KPD 0005+5106 is a He-rich DO WD, the accreted material must be He-rich as well; otherwise the WD's atmosphere will be over-polluted with H. While a Jupiter-like planet can easily provide the material to be accreted to power the hard X-ray emission, it is not clear how such a planet can survive the stellar evolution and what its chemical composition

would be. It is also not clear how an extremely low-mass star companion gets so close to a WD whose initial mass may be  $\sim 3 M_\odot$  (Kalirai et al. 2005). Binary star evolution needs to be considered for the progenitor of this system.

## 6. SUMMARY AND CONCLUSION

Three types of X-ray sources are commonly associated with WDs: soft photospheric emission, harder X-ray emission from a stellar companion with coronal activity, and accretion powered X-ray emission. It has been puzzling that a small number of apparently single WDs are associated with X-ray emission peaking near 1 keV. The two most conspicuous cases are the central star of the Helix Nebula and KPD 0005+5106.

With an effective temperature of 200,000 K, KPD 0005+5106 is a bright soft X-ray source even detected in the ROSAT All Sky Survey, and a pointed longer observation reveal an additional harder X-ray component peaking near 1 keV. We obtained Chandra X-ray Observatory observations of KPD 0005+5106 and confirmed the spatial coincidence of the hard and soft X-ray emission components with the WD. The very bright soft X-ray emission caused photon pileup, rendering the spectral analysis of the hard X-ray emission unreliable. We have thus obtained XMM-Newton X-ray observations of KPD 0005+5106 and two other WDs, PG 1159-035, and WD 0121-756, whose ROSAT observations detected  $\sim 10$  photons with energies near 1 keV. The XMM-Newton observations show these three WDs have similar X-ray spectral shapes with a bright soft component below 0.5 keV and a harder component peaking near 1 keV, and all three spectra are best fitted by models consisting of a blackbody component for the stellar photospheric emission, a thermal plasma emission component, and a power-law component. The hard X-ray luminosities in the 0.6-3.0 keV band are  $3.9 \times 10^{30}$ ,  $3.9 \times 10^{29}$ , and  $3.2 \times 10^{30}$  ergs  $s^{-1}$  for KPD 0005+5106, PG 1159-035, and WD 0121-756, respectively.

The XMM-Newton EPIC-pn observations of KPD 0005+5106 detected adequate counts for lightcurve analysis. The lightcurve in the soft energy band (0.3-0.5 keV) is essentially constant, but the lightcurve in the hard energy band (0.6-3.0 keV) shows variations with an apparent period of  $\sim 5$  hr. The hard-band lightcurve of KPD 0005+5106 extracted from the Chandra ACIS-S data also shows a similar period. We have thus computed generalized Lomb-Scargle periodograms for the XMM-Newton and Chandra lightcurves in the hard energy band both individually and combined. We find the combined lightcurve, covering 4.6 cycles, provides

the most robust period,  $4.7 \pm 0.3$  hr, with a false alarm probability of 0.41%.

The observed hard X-ray emission cannot arise from a single WD's photosphere. Infrared observations of KPD 0005+5106 place stringent constraints on possible companions – must be later and less massive than an M8 V star. Assuming that the  $4.7 \pm 0.3$  hr period in the hard X-ray light curve corresponds to a binary orbital period, we considered a  $0.075 M_{\odot}$  M9 V star, a  $0.035 M_{\odot}$  T brown dwarf, and a  $0.001 M_{\odot}$  Jupiter-like planet as the companion. We find the Jupiter-like planet exceeds the Roche radius and can be a donor providing material to be accreted by the WD to power the hard X-ray emission. The M9 V star and T brown dwarf, being photoionized and heated by the 200,000 K KPD 0005+5106 at a distance of  $\sim 1.3 R_{\odot}$ , may be inflated and the outermost material may pass the Roche radius and be accreted by the WD. We conclude that the hard X-ray emission from apparently single WDs is powered by accretion from sub-stellar companions or giant planets, and is modulated by the orbital motion with a period of  $4.7 \pm 0.3$  hr.

#### ACKNOWLEDGMENTS

We thank Dr. L. Townsley and Dr. P. Broos for advising us on the pileup effects in Chandra data, and Dr. K. Werner for critically reading this paper. This research was supported by the NASA grants SAO GO8-9026 (Chandra) and JPL 1319342 (Spitzer). Y.H.C. acknowledges grants MOST 108-2112-M-001-045 and MOST 109-2112-M-001-040 from the Ministry of Science and Technology of Taiwan, Republic of China. J.A.T. and M.A.G. are funded by UNAM DGAPA PAPIIT project IA100318. M.A.G. also acknowledges support from grant PGC2018-102184-B-IOO of the Spanish Ministerio de Ciencia, Educación y Universidades cofunded by FEDER funds. This paper has used observations made with the Italian Telescopio Nazionale Galileo (TNG) operated on the island of La Palma by the Fundación Galileo Galilei of the INAF (Istituto Nazionale di Astrofisica) at the Spanish Observatorio del Roque de los Muchachos of the Instituto de Astrofísica de Canarias.

*Software:* CIAO (v4.11; Fruscione et al. 2006), SAS (v17.0; Gabriel et al. 2004), MOPEX (Makovoz & Marleau 2005), IRAF (Tody 1986, Tody 1993), XSPEC (v12.10.1; Arnaud 1996)

## REFERENCES

- Aller, A., Lillo-Box, J., Jones, D., et al. 2020, *A&A*, in press
- Arnaud, K. A. 1996, *Astronomical Data Analysis Software and Systems V*, 101, 17
- Bilíková, J., Chu, Y.-H., Gruendl, R. A., & Maddox, L. A. 2010, *AJ*, 140, 1433 (Paper III)
- Bohlin, R. C., Savage, B. D., & Drake, J. F. 1978, *ApJ*, 224, 132
- Chu, Y.-H., Gruendl, R. A., Williams, R. M., Gull, T. R., & Werner, K. 2004a, *AJ*, 128, 2357
- Chu, Y.-H., Guerrero, M. A., Gruendl, R. A., & Webbink, R. F. 2004b, *AJ*, 127, 477 (Paper II)
- Ciardullo, R., Bond, H. E., Sipior, M. S., et al. 1999, *AJ*, 118, 488
- Downes, R. A., Liebert, J., & Margon, B. 1985, *ApJ*, 290, 321
- Drake, J. J., & Werner, K. 2005, *ApJ*, 625, 973
- Dreizler, S., & Heber, U. 1998, *A&A*, 334, 618
- Eggleton, P. P. 1983, *ApJ*, 268, 368
- Fazio, G. G., Hora, J. L., Allen, L. E., et al. 2004, *ApJS*, 154, 10
- Fleming, T. A., Schmitt, J. H. M. M., & Giampapa, M. S. 1995, *ApJ*, 450, 401
- Fleming, T. A., Werner, K., & Barstow, M. A. 1993, *ApJL*, 416, L79
- Fruscione, A., McDowell, J. C., Allen, G. E., et al. 2006, *Proc. SPIE*, 62701V
- Gabriel, C., Denby, M., Fyfe, D. J., et al. 2004, *Astronomical Data Analysis Software and Systems (ADASS) XIII*, 314, 759
- Gaia Collaboration, Brown, A. G. A., Vallenari, A., et al. 2018, *A&A*, 616, A1
- Güdel, M. 2004, *A&A Rv*, 12, 71.  
doi:10.1007/s00159-004-0023-2
- Guerrero, M. A., Chu, Y.-H., Gruendl, R. A., Williams, R. M., & Kaler, J. B. 2001, *ApJL*, 553, L55
- Kalirai, J. S., Richer, H. B., Reitzel, D., et al. 2005, *ApJL*, 618, L123
- Kaltenegger, L., & Traub, W. A. 2009, *ApJ*, 698, 519
- Kirkpatrick, J. D., & McCarthy, D. W., Jr. 1994, *AJ*, 107, 333
- Longstaff, E. S., Casewell, S. L., Wynn, G. A., et al. 2019, *MNRAS*, 484, 2566
- Makovoz, D. & Marleau, F. R. 2005, *PASP*, 117, 1113.  
doi:10.1086/432977
- McCook, G. P., & Sion, E. M. 1999, *ApJS*, 121, 1
- Mullally, F., Kilic, M., Reach, W. T., Kuchner, M. J., von Hippel, T., Burrows, A., & Winget, D. E. 2007, *ApJS*, 171, 206
- O'Dwyer, I. J., Chu, Y.-H., Gruendl, R. A., Guerrero, M. A., & Webbink, R. F. 2003, *AJ*, 125, 2239 (Paper I)
- Patten, B. M., Stauffer, J. R., Burrows, A., et al. 2006, *ApJ*, 651, 502
- Rieke, G. H., Young, E. T., Engelbracht, C. W., et al. 2004, *ApJS*, 154, 25
- Schmidt-Kaler, Th. 1982, *Landolt-Börnstein: Numerical Data and Functional Relationships in Science and Technology*, edited by K. Schaifers and H. H. Voigt (Springer-Verlag, Berlin), VI/2b
- Schwope, A. D., Staude, A., Koester, D., et al. 2007, *A&A*, 469, 1027
- Serber, A. V. 1990, *AZh*, 67, 582
- Stelzer, B., de Martino, D., Casewell, S. L., et al. 2017, *A&A*, 598, L6
- Thomas, J. H., Markiel, J. A., & van Horn, H. M. 1995, *ApJ*, 453, 403
- Tody, D. 1986, *Proc. SPIE*, 627, 733. doi:10.1117/12.968154
- Tody, D. 1993, *Astronomical Data Analysis Software and Systems (ADASS) II*, 52, 173
- van Teeseling, A., Reinsch, K., & Beuermann, K. 1996, *A&A*, 307, L49
- Wassermann, D., Werner, K., Rauch, T., & Kruk, J. W. 2010, *A&A*, 524, A9
- Weisskopf, M. C., Wu, K., Trimble, V., O'Dell, S. L., Elsner, R. F., Zavlin, V. E., & Kouveliotou, C. 2007, *ApJ*, 657, 1026
- Werner, K., Dreizler, S., Heber, U., Rauch, T., Fleming, T. A., Sion, E. M., & Vauclair, G. 1996, *A&A*, 307, 860
- Werner, K., Heber, U., & Fleming, T. 1994, *A&A*, 284, 907
- Werner, K., Rauch, T., & Kruk, J. W. 2007, *A&A*, 474, 591
- Werner, K., Rauch, T., & Kruk, J. W. 2008, *A&A*, 492, L43
- Werner, K., Wolff, B., Pakull, M. W., et al. 1996, *Supersoft X-ray Sources*, 131
- Wilms, J., Allen, A., & McCray, R. 2000, *ApJ*, 542, 914
- Zechmeister, M., & Kürster, M. 2009, *A&A*, 496, 577